CrossMark

An Alternative Frictional Boundary Condition for Computational Fluid Dynamics Simulation of Friction Stir Welding

Gaoqiang Chen, Zhili Feng, Yucan Zhu, and Qingyu Shi

For better application of numerical simulation in optimization and design of friction stir welding (FSW), this paper presents a new frictional boundary condition at the tool/workpiece interface for computational fluid dynamics (CFD) modeling of FSW. The proposed boundary condition is based on an implementation of the Coulomb friction model. Using the new boundary condition, the CFD simulation yields non-uniform distribution of contact state over the tool/workpiece interface, as validated by the experimental weld macrostructure. It is found that interfacial sticking state is present over large area at the tool-workpiece interface, while significant interfacial sliding occurs at the shoulder periphery, the lower part of pin side, and the periphery of pin bottom. Due to the interfacial sticking, a rotating flow zone is found under the shoulder, in which fast circular motion occurs. The diameter of the rotating flow zone is smaller than the shoulder diameter, which is attributed to the presence of the interfacial sliding at the shoulder periphery. For the simulated welding condition, the heat generation due to friction and plastic deformation makes up 54.4 and 45.6% of the total heat generation rate, respectively. The simulated temperature field is validated by the good agreement to the experimental measurements.

1. Introduction

Friction stir welding (FSW) (Ref 1, 2) is an advanced materials manufacturing technology, which has wide applications such as joining of similar/dissimilar alloys (Ref 1, 3) and synthesis of particle-reinforced bulk composites (Ref 4). In FSW process, a rotating welding tool is in intimate contact with the workpiece, which generates large interfacial friction between the tool and the workpiece. The interfacial friction leads to significant heat generation (Ref 5-7), high temperature (Ref 8), and significant plastic flow (Ref 9, 10). Such thermal-mechanical processes induced by the interfacial friction play important roles in shaping the microstructure (Ref 1) and thus the final in-use properties of the joints. Numerical simulation (Ref 11-17) has proved to be a very successful approach in quantitative investigation of the thermal-mechanical processing condition in FSW for the purpose of fundamental understanding and optimal design.

Computational fluid dynamics (CFD) is one of the most widely applied computational approaches in the numerical simulation of FSW. Colegrove et al. (Ref 14, 15) were among the first to develop three-dimensional numerical simulation based on the CFD, to study the material flow and temperature distribution in FSW of aluminum alloys using both smooth and threaded welding tool. Nandan et al. (Ref 16) developed a CFD model for FSW of a mild steel to analyze the heat generation, heat transfer, and plastic flow in the welding process. In recent researches, the CFD simulation has been successfully applied in the studying the spatial distribution of heat generation flux (Ref 6, 7) and the effects of tool profile on the material flow (Ref 18-20).

In the CFD-based simulation for FSW, one of the critical issues is the frictional boundary condition between the welding tool and the workpiece. In the previous simulation, the frictional boundary condition at the tool/workpiece interface could be divided into two categories: (a) velocity-based boundary condition and (b) shear stress-based boundary condition. The most important consideration in the frictional boundary condition is the determination of the contact state (Ref 5), i.e., the sliding/sticking state. In a number of the simulation studies (Ref 6, 15, 19), the sticking contact state was employed via a velocity-based boundary condition, in which the material was assumed to flow at the same velocity as the welding tool at the tool/workpiece interface. Generally, both the maximum temperature and the deformation zone size were over-predicted using the 'sticking' condition (Ref 15). This is because it is unrealistic to justify that the workpiece material at the interface would flow at the same velocity as the tool for various welding conditions.

Gaoqiang Chen, The State Key Laboratory of Tribology, Tsinghua University, 1 Tsinghua Yuan Park, Haidian, Beijing 100084, Peoples Republic of China; Key Laboratory for Advanced Materials Processing Technology, Department of Mechanical Engineering, Tsinghua University, 1 Tsinghua Yuan Park, Haidian, Beijing 100084, Peoples Republic of China; and Materials Science & Technology Division, Oak Ridge National Laboratory, 1 Bethel Valley Road, Oak Ridge, TN 37831; **Zhili Feng**, Materials Science & Technology Division, Oak Ridge National Laboratory, 1 Bethel Valley Road, Oak Ridge, TN 37831; and **Yucan Zhu** and **Qingyu Shi**, The State Key Laboratory of Tribology, Tsinghua University, 1 Tsinghua Yuan Park, Haidian, Beijing 100084, Peoples Republic of China; Key Laboratory for Advanced Materials Processing Technology, Department of Mechanical Engineering, Tsinghua University, 1 Tsinghua Yuan Park, Haidian, Beijing 100084, Peoples Republic of China. Contact e-mails: Gaoqiang.chen@hotmail.com and shqy@tsinghua.edu.cn.

Indeed, it was shown by the Qian et al's experiments (Ref 21) that the transition between the sliding and sticking could occur at least at certain welding condition. In order to include the interfacial sliding, Atharifar et al. (Ref 22) assumed a sliding state at the tool/workpiece interface using the velocity boundary condition, in which the interfacial material velocity is artificially defined as 60% of the tool velocity to investigate the loads carried by tool during FSW. Nandan et al. (Ref 16) proposed an empirical equation to determine the velocity profile at the tool/workpiece interface in FSW of mild steel, which resulted in more reasonable prediction of the deformation zone in the weld. Wang et al. (Ref 23) used a contact shoulder radius ratio (CSRR) to determine the proportion of the tool shoulder that interfacial sticking was present. It could be known from these research that, for the simulation using a velocity-based boundary condition, it is necessary to determine a proper velocity profile at the tool/workpiece interface considering the interfacial sliding/sticking, in order to reasonably predict the fluid flow behaviors during FSW. However, there was no generic way for quantitative description of the interfacial contact state for various welding parameters, tool geometries, and materials. In recent CFD simulations, the shear stress-based boundary condition has been demonstrated to superior to a velocity-based boundary condition in the CFD simulation of FSW (Ref 24). Using the shear stress-based boundary condition, the interfacial material velocity is calculated based on the balance of interfacial shear stresses, instead of predetermining the interfacial velocity profile. Liechty et al. (Ref 24) used a shear stress-based boundary condition in a simulation for the FSW of plasticine. Chen et al. (Ref 25) applied the shear stress-based boundary condition in their model for FSW of AA6061 using a threaded welding tool, which resulted in reasonable prediction of the thermal-mechanical processing condition. Unfortunately, the shear stress-based boundary condition used in the current simulation (Ref 24, 25) was proposed based on the assumption of the sliding state. The presence of 'sticking' state at the tool/workpiece, which is considered to be of critical importance in understanding the thermal-mechanical condition in FSW (Ref 9, 11), could not be predicted in the current simulation. This limits the application of numerical simulation in optimization and design of the weld process. Therefore, it is of great interest to implement a generic shear stress boundary condition in the CFD simulation for FSW, which is capable to predict the presence of both the sliding state and the sticking state at the tool/workpiece interface.

In this study, we present an alternative shear stress-based frictional boundary condition for the CFD simulation of FSW. In the proposed boundary condition, the transition between the sliding state and sticking state at the tool/workpiece interface is taken into consideration. In this paper, the CFD simulation approaches and the implementation of the new boundary condition are described in details. By the numerical simulation, the variation of the contact state over the tool/workpiece interface, as well as its effect on the heat generation and material flow pattern, are discussed. In addition, the weld macrostructure and the measured temperatures curves from the FSW experiments are used to validate the computational approaches.

2. Experiments

FSW butt joining of two AA2024-T4 sheets was conducted. The dimensions of each workpiece were 145 mm × 55 mm ×

3 mm (length × width × thickness). The welding tool was made by H13 steel. The tool shoulder was 13 mm in diameter, and length of the conical pin was 2.4 mm. The radius of pin was 2 mm at the root and 1.75 mm at the tip. In the welding process, the FSW tool rotated at 1600 rpm and the workpiece traveled at 20 mm/min. No tilt angle was employed in the experiment. The plunge depth was 0.5 mm. The length of the weld was 100 mm. The temperature history was recorded by six K-type thermal couples located 3, 6, and 9 mm from the welding centerline in the mid-thickness plane on advancing side (AS) and retreating side (RS). A specimen was cut after welding for examination of the cross-sectional macrostructure. The specimen was grounded, polished, and etched with Keller's solution (95 mL water, 1.5 mL hydrochloric acid, 2.5 mL nitric acid, 1 mL hydrofluoric acid) for 1 min. After that, the macrostructure of specimen was observed by optical microscope.

3. Frictional Boundary Condition at the Tool/Workpiece Interface

The proposed frictional boundary condition is based on a straightforward theoretical approach developed by Mostaghel and Davis (Ref 26) for dynamic analysis of many friction problems, such as earthquake. In order to mathematically model the dynamic sliding/sticking transition in the friction model, it is key to include the adaption of frictional stress caused by the transition, as the frictional stress in the sliding state and state is different. For the sliding state illustrated in Fig. 1(a), the frictional stress is determined by the interfacial normal stress and the friction coefficient based on the Coulomb friction law. For the sticking state, the interfacial relative motion is eliminated because the maximum friction is larger
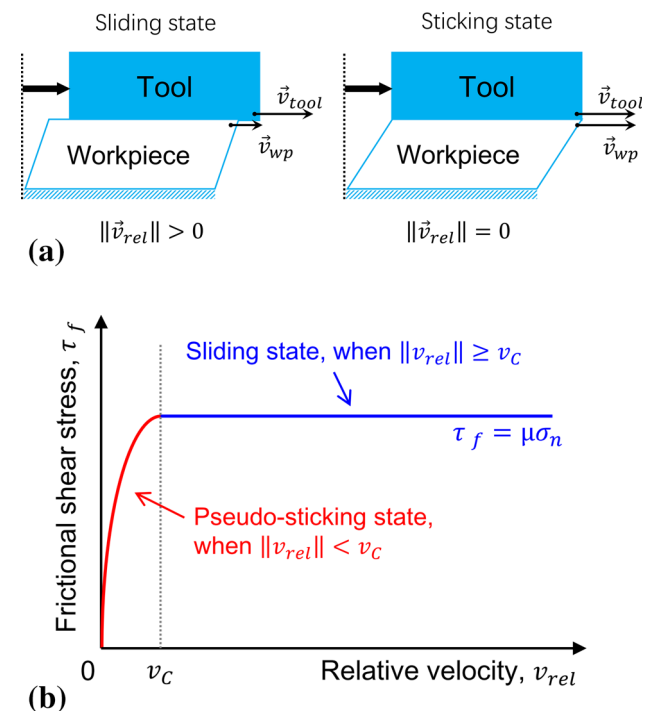

Fig. 1 The interfacial friction model. (a) Illustration for the interfacial contact state (b) Definition of the interfacial friction stress

than the necessary force to keep the interfacial workpiece velocity the same as the tool velocity. In presence of the sticking state, the interfacial friction is self-adapted to the necessary force for keeping the sticking state.

Figure 1(b) shows the frictional stress as a function of the interfacial relative velocity in the proposed model. In the sliding state, the frictional stress is determined by the Coulomb friction law (Ref 27). A pseudo-sticking state is used instead of implementing a perfect sticking state. The pseudo-sticking state is reached when the magnitude of the relative velocity is less than a critical small value, v_C. The adaption of the frictional stress in the pseudo-sticking state is modeled by a smooth function. This is a common approach to capture the friction-induced sliding/sticking transition with acceptable computational costs (Ref 26). Mathematically, the frictional stress, $\vec{\tau}_f$ is defined by three terms, which are the magnitude term, the direction term, and the pseudo-sticking term, given by

$$\vec{\tau}_f = M \cdot \vec{D} \cdot \beta_S. \tag{Eq 1}$$

M is the magnitude term, which defines the magnitude of the frictional stress in the sliding state, given by,

$$M = \mu_f \sigma_n, \tag{Eq 2}$$

where μ_f is the frictional coefficient (taken as 0.25 (Ref 27)), and σ_n is the interfacial normal stress (taken as 50 MPa (Ref 27)). $\vec{D}$ is the direction term. Given the direction of the frictional stress is the same as the direction of the relative velocity, $\vec{D}$ is defined by,

$$\vec{D} = \begin{cases} \vec{v}_{\text{rel}}/\|\vec{v}_{\text{rel}}\|, & \text{if} \quad \vec{v}_{\text{rel}} \neq 0 \\ 0, & \text{if} \quad \vec{v}_{\text{rel}} = 0 \end{cases} \tag{Eq 3}$$

where $\vec{v}_{\text{rel}}$ is the interfacial relative velocity defined by $\vec{v}_{\text{rel}} = \vec{v}_{\text{tool}} - \vec{v}_{\text{wp}}$, $\vec{v}_{\text{tool}}$ is the tool velocity and $\vec{v}_{\text{wp}}$ is the workpiece velocity at the interface. β_S is the pseudo-sticking term to implement the smooth adaption of the frictional stress due to the sliding/sticking transition. β_S is given as (Ref 26)

$$\beta_S = \tan h\left(\alpha \cdot \|\vec{v}_{\text{rel}}\|\right), \tag{Eq 4}$$

where α is a scaling constant. We found that $\alpha = 50$ s/m worked well in our tests. The critical velocity v_C is determined as $\sim$0.04 m/s, which is very small comparing to the typical tool velocity ($\sim$1.00 m/s).

4. Approaches in the CFD Simulation

4.1 Assumptions

The workpiece is taken as an incompressible single-phase fluid with non-Newtonian viscosity. The density of workpiece metal is taken as a constant, while the thermal conductivity and the specific heat are temperature dependent. In addition, the thermal-mechanical process in the quasi-steady state welding process is considered, while the highly transient process at the beginning and end of welding are ignored.

4.2 Governing Equations

The continuity equation and momentum conservation equation for incompressible single-phase flow are given by

$$\frac{\partial \rho}{\partial t} + \nabla \cdot (\rho \vec{v}) = 0, \tag{Eq 5}$$

$$\frac{\partial \rho \vec{v}}{\partial t} + \nabla \cdot (\rho \vec{v} \vec{v}) = -p + \nabla \cdot \left(\mu\left(\nabla \vec{v} + \nabla \vec{v}^T\right)\right), \tag{Eq 6}$$

where ρ is the density of fluid, μ is the temperature-and-strain rate-dependent viscosity, p is the pressure, $\vec{v}$ is the fluid velocity vector, and t is the flow time.

The energy conservation equation is given by

$$\frac{\partial \rho H}{\partial t} + \nabla \cdot (\rho \vec{v} H) = \nabla \cdot (k \nabla T) + S_V, \tag{Eq 7}$$

where H is the enthalpy, T is the temperature, k is the thermal conductivity, and S_V is the spatial source term regarding the volumetric heat flux due to plastic deformation. The enthalpy H is given by

$$H = \int_{T_{ref}}^{T} C_P \mathrm{d}t, \tag{Eq 8}$$

where C_P is the heat capacity, T is the temperature, and T_{ref} is the reference temperature, which is defined to be room temperature, 27 °C. The conservation equations were solved, using the commercial CFD package, ANSYS Fluent 15.0 (Ref 28).

4.3 Geometric Model and Boundary Conditions

Figure 2 illustrates the geometry model in the numerical simulation. The dimensions of the workpiece and the geometry of welding tool are taken as the same as the setup in the experiment. In the numerical analysis, the finite volume method (FVM) is used to discretize and solve the governing equations. The 'Fluid zone' is meshed with 157,716 hexagonal grids. As shown by the inset in Fig. 2, relatively fine mesh is used in the vicinity of the tool in order to capture the thermomechanical phenomena with large spatial gradient in this area.

Different boundary conditions are defined for modeling of the quasi-steady state welding process, as shown in Fig. 2. An 'Inlet-outlet' method is adopted such that the material flows into the 'Fluid zone' from 'Material inlet' at the welding speed and flows out of the domain from the 'Material outlet.' At the 'Tool/workpiece interface,' the frictional shear stress and the frictional heat flux are applied, which are described below in details. The 'Back surface' and 'Sides' of the work piece are assumed to contact with the fixtures, in which the convection heat transfer coefficient on 'Back surface' and 'Sides' is defined as 500 W/m^2 K (Ref 29) to calculate the heat loss to the fixtures. The material velocity on 'Back surface' and 'Sides' is set to be the same as the welding speed. 'Top surface' is taken as a free surface contacting with air, where the shear stress is assumed to be 0 MPa and the convection heat transfer coefficient is assumed as 30 W/m^2 K (Ref 30).

4.4 Material Properties

The density of AA2024 is taken as 2705 kg/m^3 (Ref 31). The temperature-dependent thermal conductivity and specific heat for AA2024 shown in Fig. 3 are taken from Ref (Ref 31). The thermophysical properties of H13 tool steel are listed in Table 1.

The viscosity of the fluid is defined by the following formulation based on the theory of visco-plasticity (Ref 15),
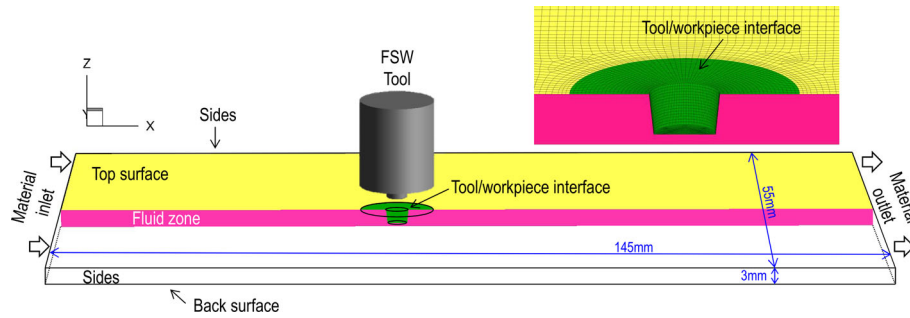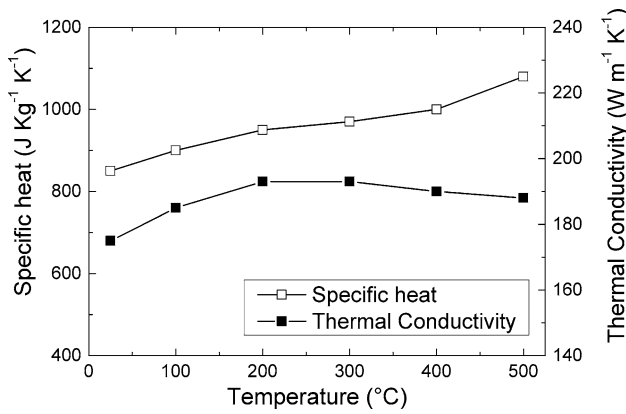
Fig. 2 Geometric model in the simulation

Fig. 3 Thermophysical properties of AA2024 (Ref 31)

Table 1 Thermophysical properties of H13 steel (Ref 32)

Parameter	Value
Thermal conductivity of H13 steel, k_T	24.4 W m^{-1} K^{-1}
Density, ρ_T	7.8×10^3 kg m^{-3}
Heat capacity, C_{PT}	0.46 J kg^{-1} K^{-1}

$$\mu = \frac{\sigma}{3\dot{\varepsilon}}, \tag{Eq 9}$$

where σ is the flow stress and $\dot{\varepsilon}$ is the effective strain rate, which is defined by

$$\dot{\varepsilon} = \sqrt{\frac{2}{3}\dot{\varepsilon}_{ij}\dot{\varepsilon}_{ij}}, \tag{Eq 10}$$

where $\dot{\varepsilon}_{ij}$ is the strain rate tensor given by

$$\dot{\varepsilon}_{ij} = \frac{1}{2}\left(\frac{\partial v_i}{\partial x_j} + \frac{\partial v_j}{\partial x_i}\right). \tag{Eq 11}$$

The thermal softening effects on the deformation resistance of AA2024 is taken into account in our simulation using a temperature-dependent flow stress, σ in Eq 9. The anisotropy (Ref 33) of the flow stress with respect to the rolling direction is ignored, as the rolled grain structure is significantly changed due to the dynamic recrystallization in FSW (Ref 34). Figure 4 shows the flow stress curve in the current model. The flow stress values are interpolated from yield strength values from Ref (Ref 35) in wide temperature range using a

non-linear interpolation. The flow stress is taken as 0 MPa if the temperature exceeds the solidus temperature of AA2024, which is 502 °C (Ref 31).

4.5 Heat Generation Model

Different from the fusion welding, the heat generation in FSW is caused by the friction at the tool/workpiece interface and the plastic deformation of material. As such, the heat generation in FSW is fully coupled with the simultaneous material flow around the welding tool. The heat generation by the interfacial friction is determined by the interfacial frictional stress and the interfacial sliding velocity, while the heat generation due to the plastic deformation is determined by the flow stress and the strain rate. In our simulation, heat generation due to friction is taken as a facial heat flux at the tool/workpiece interface, which is determined by the frictional shear stress and the relative velocity between tool and workpiece, given by

$$q_f = \eta \cdot \|\vec{\tau}_f\| \cdot \|\vec{v}_{rel}\|, \tag{Eq 12}$$

where $\vec{\tau}_f$ is the frictional shear stress defined as same as Eq 1 and $\vec{v}_{rel}$ is the interfacial relative velocity between tool and workpiece. η is the fraction of frictional heat flux into the workpiece given by (Ref 36)

$$\eta = \frac{\sqrt{(k\rho C_P)_W}}{\sqrt{(k\rho C_P)_W + (k\rho C_P)_T}}, \tag{Eq 13}$$

where k is the thermal conductivity, ρ is the density, C_P is the heat capacity, the subscripts W and T denote the workpiece and the tool, respectively. Based on the data in Table 1 and Fig. 3, η is calculated as 0.71 in the current simulation.

The heat generated from plastic deformation is considered as a volumetric heat flux, taken as a source term S_V in the conservation equation of energy (Eq 3). The heat flux is calculated by the product of the flow stress and the plastic deformation rate, given as

$$q_p = \kappa \cdot \sigma \cdot \dot{\varepsilon}, \tag{Eq 14}$$

where $\kappa = 0.6$ (Ref 2) is the fraction of plastic work dissipated as heat, σ is the flow stress and $\dot{\varepsilon}$ is the effective strain rate.

4.6 Numerical Solution Procedure

In the CFD model above mentioned, the heat generation, temperature, and material flow are thermal-mechanical fully coupled. The model is solved in a transient procedure. First, the temperature and material velocity are initialized as 300 K and 0.00 m/s respectively. Second, the numerical calculation is
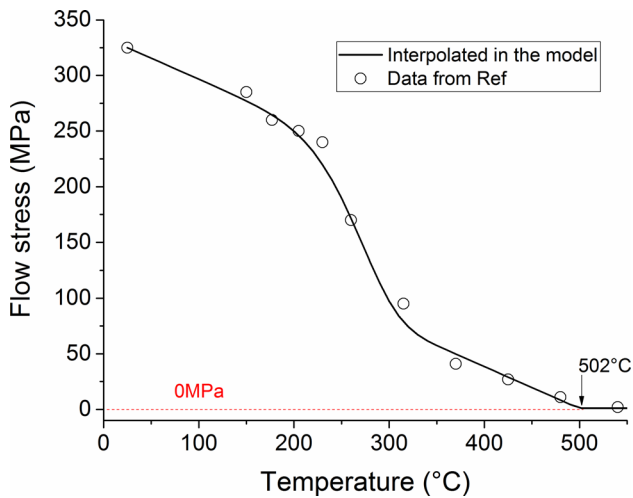
Fig. 4 Temperature-dependent flow stress of AA2024. (Ref [35])

Fig. 5 The predicted velocity of the workpiece at tool/workpiece interface (Color figure online)

conducted with a time step of 0.02 s. Third, a quasi-steady state is reached at 40 s as little change is found in the temperature field and material flow velocity field. Therefore, the temperature and material flow field at 40 s are outputted for analysis.

5. Results and Discussion

5.1 Contact State at the Tool/Workpiece Interface

Based on the proposed frictional boundary condition, the contact state at the tool/workpiece interface is provided. Figure 5 shows the predicted workpiece velocity at the tool/workpiece interface. It is shown that the predicted distribution of material velocity is almost symmetric about the tool axis. In order to analyze the interfacial contact state, the velocity of the workpiece at the position shown by dashed line (*oabc* in Fig. 5) is plotted versus the distance from tool axis in Fig. 6, in comparison with the tool velocity. It could be seen from Fig. 5 and 6 that the contact state is non-uniformly distributed over the tool/workpiece interface in the simulated welding condition. The sticking state is present at inner part of the shoulder surface, upper part of the pin side, and most part of the pin bottom surface as the interfacial velocity of the workpiece is almost the same as the tool velocity. Owing to the interfacial sticking, the maximum workpiece velocity is found to be 793 mm/s at the shoulder/workpiece interface. Significant interfacial sliding occurs at the shoulder periphery, the lower part of pin side, and the periphery of pin bottom. Due to the interfacial sliding at the shoulder periphery, the minimum velocity of workpiece on the shoulder surface is found to be 0.34 mm/s at the shoulder periphery (point-c), which is almost the same as the travel speed (0.33 mm/s) of workpiece during the welding. Significant interfacial sliding also occurs at the lower part of the pin side, which results in a small velocity of 48.5 mm/s at the pin bottom edge (point-a).

It is worth noting that the predicted locations of the maximum material velocity are different between the current simulation and the published work (Ref [6], [20]) with a velocity boundary condition. As shown in Fig. 5 and 6, due to the significant interfacial sliding at the shoulder periphery, the maximum velocity does not appear at the shoulder periphery,
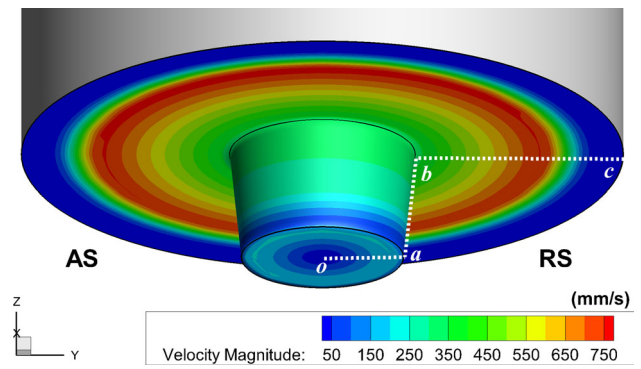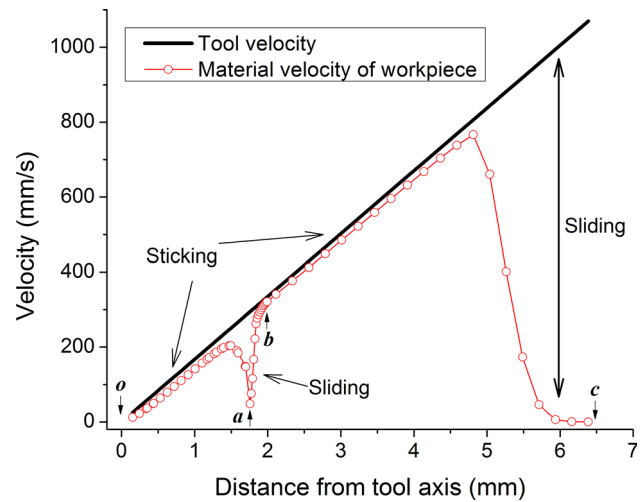

Fig. 6 Velocity profile at the tool/workpiece interface

but at a location 1.3 mm away from the periphery. In comparison, the maximum of material velocity was located at the shoulder periphery in the simulations (Ref [6], [20]) with a velocity boundary condition.

The non-uniform distribution of the contact state over the tool/workpiece interface is important in interpreting the formation of the weld macrostructure. The cross-sectional weld macrostructure from the experiment is shown in Fig. 7. As marked by the fine dash line, the stir zone (SZ) and thermal-mechanically affected zone (TMAZ) are typical microstructural feature in friction stir welds. The formation of the SZ and the TMAZ is considered to be relate to the material flow during FSW. As shown in Fig. 7, the size of the SZ in the upper region of the weld is much wider than that in the lower region, which is a common microstructural feature in the friction stir welds (Ref [9], [37]). The variation of the SZ size could be explained by the variation of the interfacial contact state. In the upper region, high rate plastic flow is induced due to the interfacial sticking between the welding tool and the workpiece; as a result, the size of SZ is much larger than the pin size. In the lower region of the weld, the width of the SZ is similar to the pin size, because large extent of interfacial sliding occurs on the lower region of the pin side. Furthermore, it is interesting to note that the thickness of the SZ and the TMAZ decreases significantly at the shoulder periphery (marked by letter A). This could be
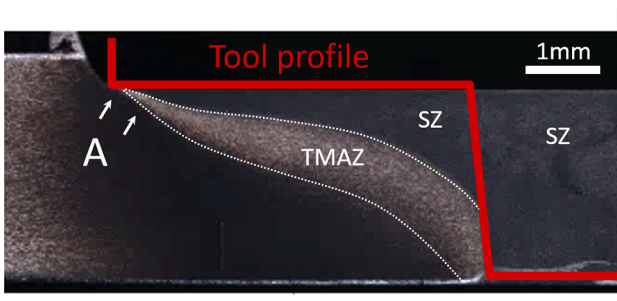
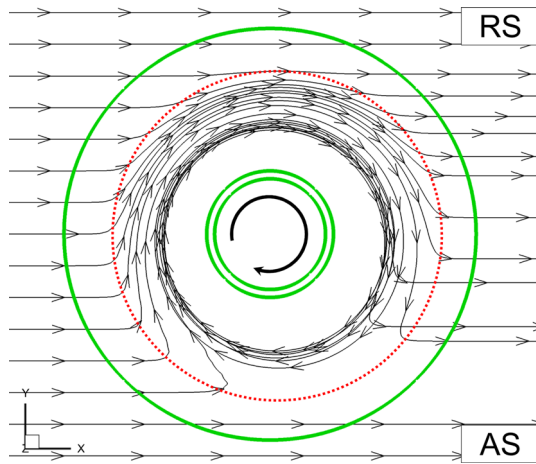**Fig. 7** Weld macrostructure on advancing side

Fig. 8 Material flow paths under the welding tool (0.6 mm below the shoulder surface)

explained by the reduction in the interfacial velocity at shoulder periphery due to the interfacial sliding as shown in Fig. 5.

5.2 Material Flow Pattern

Figure 8 shows the predicted flow paths in different horizontal planes located at 0.6 mm away from the tool shoulder. It is found that a rotating flow zone (RFZ) exists in the vicinity of the shoulder as marked by red dotted lines in Fig. 8. The presence of such a RFZ under the shoulder is supported by the experiments by Schmidt et al. (Ref 10) and the recent in situ observation by Morisada et al. (Ref 38). In their study, a similar RFZ is found to be smaller than the shoulder, in which the material is undergoing fast circular motion. Both the in situ observation and our simulation result show that the material enters the RFZ in front of the tool and flows around the tool for several circles before depositing behind the tool. As such, the RFZ is a channel for rapid material transportation from the front of the tool to the behind. As shown in Fig. 8, the shape of RFZ is almost circulate in the *X-Y* plane. The diameter of the RFZ is smaller than the shoulder diameter, which is attributed to the interfacial sliding state at the shoulder periphery. It is worth noting that the sliding state at the shoulder periphery may play an important role in the formation of a friction stir weld. As the material is undergoing fast circular motion in the RFZ, excessive loss of the material may be caused due to the centrifugal motion, if the size of the RFZ reaches or exceeds the shoulder diameter with the absence of the interfacial sliding at the shoulder periphery.

5.3 Heat generation and Temperature

The spatial distribution of the heat generation flux is critical in understanding and controlling of the temperature field in a welding process. The transition between the sliding and
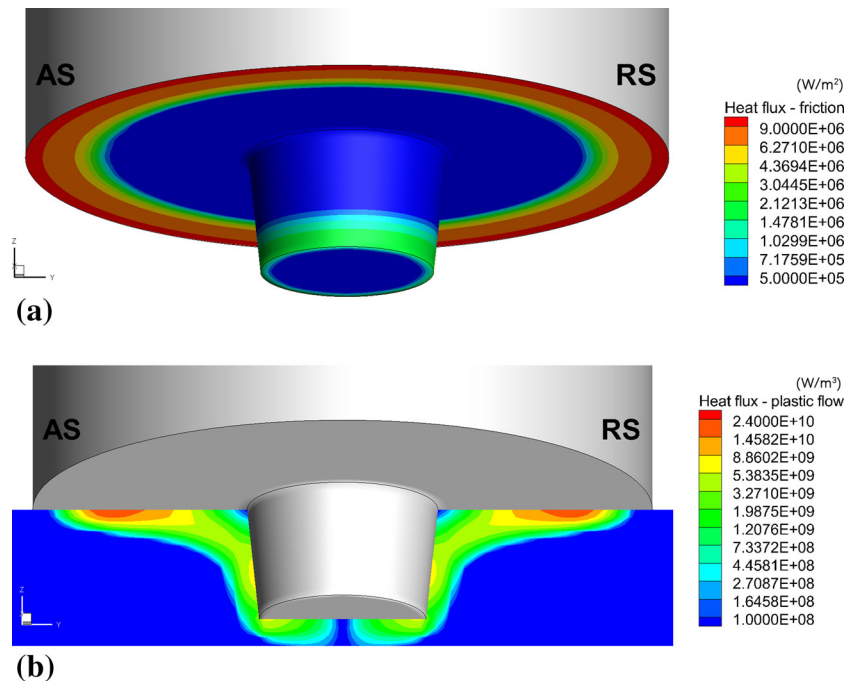

Fig. 9 Heat generation rate. (a) Heat flux by interfacial friction. (a) Heat flux by plastic deformation (Color figure online)
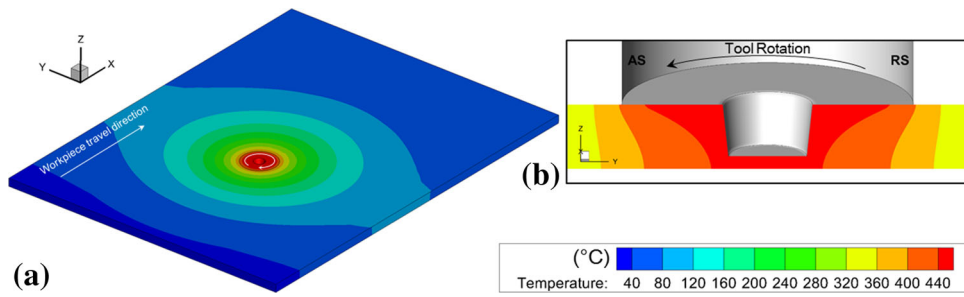
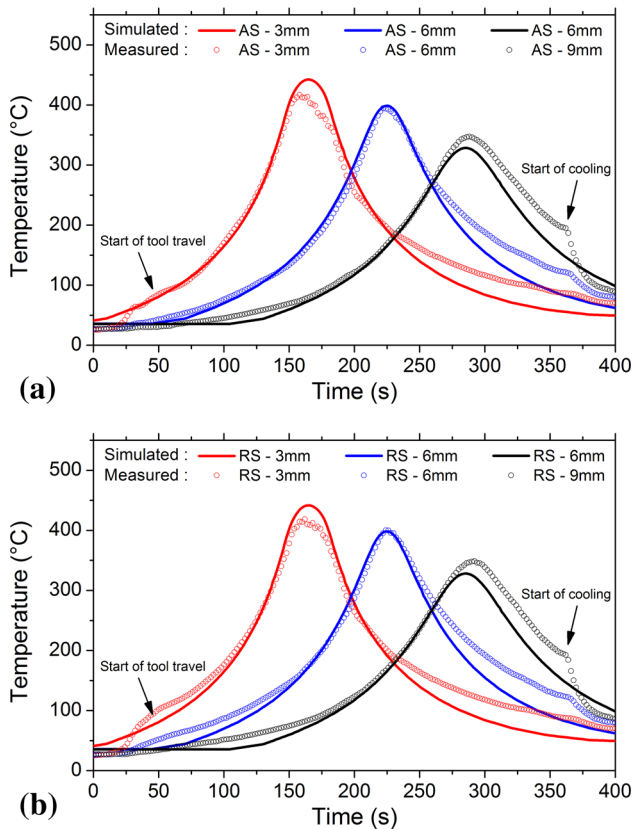**Fig. 10** Predicted temperature field (Color figure online)

Fig. 11 Predicted and measured temperature histories. (a) Advancing side. (b) Retreating side (Color figure online)

sticking state at the tool/workpiece interface has major impact on heat generation flux distribution during FSW. The predicted heat generation fluxes are shown in Fig. 9. Figure 9(a) shows the facial heat flux by the interfacial sliding friction, and Fig. 9(b) shows the volumetric heat flux by plastic deformation in the vicinity of the welding tool. At the inner part of the shoulder, the upper part of the pin side and the pin bottom, little heat is generated by friction, and large amount of heat is generated by plastic deformation owing to the presentation of the sticking state. At the shoulder periphery and the lower part of the pin side, owing to the presentation of the sliding state, large amount of frictional heat is generated because of the large relative velocity.

In addition, knowing the sliding/sticking state at the tool/workpiece interface is important for the analysis of the

contribution of friction and plastic deformation to the total heat generation in FSW. By integrating the frictional heat flux and plastic deformation heat flux over the computing domain in the current numerical simulation, the total heat generated from friction and plastic deformation is 424.8 and 355.4 W, respectively, for the simulated welding conditions, which makes up 54.4 and 45.6% of the total heat generation rate, respectively. The current frictional boundary condition yields more reasonable heat flux partition than the 'sticking' velocity boundary condition (Ref 6), where all the heat is assumed to be generated by plastic deformation.

The predicted temperature field on the workpiece is shown in Fig. 10(a). The temperature is relatively high in the vicinity of the tool due to the localized heat generation. It could be found that the temperature contour lines on the top surface are close to circular as the welding speed in the present research is relatively slow, which is 20 mm/min. Figure 10(b) shows the temperature distribution at the cross-section under the tool. A bowl-shaped localized high temperature volume, in which the temperature exceeds 400 °C, exists in the vicinity of the tool/workpiece interface. For verification purpose, the simulated and measured temperature curves in the locations, which are 3, 6, and 9 mm away from the welding center on both AS and RS in the mid-thickness plane, are plotted in Fig. 11(a) and (b). It can be found that the simulated temperature distribution is accurate, as the simulated temperature curve agrees quite well with the experimental measurements.

6. Conclusions

1. An alternative frictional boundary condition is proposed and demonstrated for the CFD simulation of FSW in consideration of the transition between sliding state and sticking state at the interface between the welding tool and workpiece.
2. Non-uniform distribution of the contact state over the tool/workpiece interface is predicted by the proposed CFD simulation and validated by the experimental weld macrostructure.
3. The non-uniform distribution of the contact state at the tool/workpiece interface has major impact on heat generation flux distribution during FSW. At the shoulder periphery, large amount of frictional heat is generated due to interfacial sliding, while heat is mainly generated by the plastic deformation at the inner part. For the simulated welding condition, the heat generation due to friction and plastic deformation makes up 54.4 and 45.6% of

the total heat generation rate, respectively.

4. Due to the interfacial sticking, a rotating flow zone is found under the shoulder, in which fast circular motion occurs. The diameter of the RFZ is smaller than the shoulder diameter, which is attributed to the presence of the interfacial sliding at the shoulder periphery.

5. Accurate temperature distribution is simulated by the CFD simulation based on the proposed boundary condition. The simulated temperature curves agree well with the experimental measurements.

References

1. R.S. Mishra and Z.Y. Ma, Friction Stir Welding and Processing, *Mater. Sci. Eng.: R: Rep.*, 2005, **50**(1–2), p 1–78

2. R. Nandan, T. DebRoy, and H. Bhadeshia, Recent Advances in Friction-Stir Welding-Process, Weldment Structure and Properties, *Prog. Mater Sci.*, 2008, **53**(6), p 980–1023

3. X. Liu, S. Lan, and J. Ni, Analysis of Process Parameters Effects on Friction Stir Welding of Dissimilar Aluminum Alloy to Advanced High Strength Steel, *Mater. Des.*, 2014, **59**, p 50–62

4. K. Sun, Q. Shi, Y. Sun, and G. Chen, Microstructure and Mechanical Property of Nano-SiCp Reinforced High Strength Mg Bulk Composites Produced by Friction Stir Processing, *Mater. Sci. Eng. A*, 2012, **547**, p 32–37

5. H. Schmidt, J. Hattel, and J. Wert, An Analytical Model for the Heat Generation in Friction Stir Welding, *Modell. Simul. Mater. Sci. Eng.*, 2004, **12**(1), p 143

6. G.-Q. Chen, Q.-Y. Shi, Y.-J. Li, Y.-J. Sun, Q.-L. Dai, J.-Y. Jia, Y.-C. Zhu, and J.-J. Wu, Computational Fluid Dynamics Studies on Heat Generation During Friction Stir Welding of Aluminum Alloy, *Comput. Mater. Sci.*, 2013, **79**, p 540–546

7. H. Su, C.S. Wu, A. Pittner, and M. Rethmeier, Thermal Energy Generation and Distribution in Friction Stir Welding of Aluminum Alloys, *Energy*, 2014, **77**, p 720–731

8. W. Tang, X. Guo, J. McClure, L. Murr, and A. Nunes, Heat Input and Temperature Distribution in Friction Stir Welding, *J. Mater. Process. Manuf. Sci.*, 1998, **7**, p 163–172

9. T. Seidel and A.P. Reynolds, Visualization of the Material Flow in AA2195 Friction-Stir Welds Using a Marker Insert Technique, *Metall. Mater. Trans. A*, 2001, **32**(11), p 2879–2884

10. H.N.B. Schmidt, T. Dickerson, and J.H. Hattel, Material Flow in Butt Friction Stir Welds in AA2024-T3, *Acta Mater.*, 2006, **54**(4), p 1199–1209

11. H. Schmidt and J. Hattel, A Local Model for the Thermomechanical Conditions in Friction Stir Welding, *Modell. Simul. Mater. Sci. Eng.*, 2005, **13**(1), p 77

12. Z. Zhang, Comparison of Two Contact Models in the Simulation of Friction Stir Welding Process, *J. Mater. Sci.*, 2008, **43**(17), p 5867–5877

13. M. Grujicic, G. Arakere, C.-F. Yen, and B.A. Cheeseman, Computational Investigation of Hardness Evolution During Friction-Stir Welding of AA5083 and AA2139 Aluminum Alloys, *J. Mater. Eng. Perform.*, 2010, **20**(7), p 1097–1108

14. P.A. Colegrove and H.R. Shercliff, Experimental and Numerical Analysis of Aluminium Alloy 7075-T7351 Friction Stir Welds, *Sci. Technol. Weld. Join.*, 2003, **8**(5), p 360–368

15. P.A. Colegrove and H.R. Shercliff, 3-Dimensional CFD Modelling of Flow Round a Threaded Friction Stir Welding Tool Profile, *J. Mater. Process. Technol.*, 2005, **169**(2), p 320–327

16. R. Nandan, G.G. Roy, T.J. Lienert, and T. Debroy, Three-Dimensional Heat and Material Flow During Friction Stir Welding of Mild Steel, *Acta Mater.*, 2007, **55**(3), p 883–895

17. D.M. Neto and P. Neto, Numerical Modeling of Friction Stir Welding Process: A Literature Review, *Int. J. Adv. Manuf. Technol.*, 2013, **65**(1), p 115–126

18. S. Ji, Q. Shi, L. Zhang, A. Zou, S. Gao, and L. Zan, Numerical Simulation of Material Flow Behavior of Friction Stir Welding Influenced by Rotational Tool Geometry, *Comput. Mater. Sci.*, 2012, **63**, p 218–226

19. Z. Yu, W. Zhang, H. Choo, and Z. Feng, Transient Heat and Material Flow Modeling of Friction Stir Processing of Magnesium Alloy Using Threaded Tool, *Metall. Mater. Trans. A*, 2012, **43**(2), p 724–737

20. H. Su, C.S. Wu, M. Bachmann, and M. Rethmeier, Numerical Modeling for the Effect of Pin Profiles on Thermal and Material Flow Characteristics in Friction Stir Welding, *Mater. Des.*, 2015, **77**, p 114–125

21. J.W. Qian, J.L. Li, J.T. Xiong, F.S. Zhang, W.Y. Li, and X. Lin, Periodic Variation of Torque and Its Relations to Interfacial Sticking and Slipping During Friction Stir Welding, *Sci. Technol. Weld. Join.*, 2012, **17**(4), p 338–341

22. H. Atharifar, D. Lin, and R. Kovacevic, Numerical and Experimental Investigations on the Loads Carried by the Tool During Friction Stir Welding, *J. Mater. Eng. Perform.*, 2009, **18**(4), p 339–350

23. H. Wang, P.A. Colegrove, and J.F. dos Santos, Numerical Investigation of the Tool Contact Condition During Friction Stir Welding of Aerospace Aluminium Alloy, *Comput. Mater. Sci.*, 2013, **71**, p 101–108

24. B.C. Liechty and B.W. Webb, Modeling the Frictional Boundary Condition in Friction Stir Welding, *Int. J. Mach. Tools Manuf*, 2008, **48**(12–13), p 1474–1485

25. G. Chen, Q. Shi, Y. Fujiya, and T. Horie, Simulation of Metal Flow During Friction Stir Welding Based on the Model of Interactive Force Between Tool and Material, *J. Mater. Eng. Perform.*, 2014, **23**(4), p 1321–1328

26. N. Mostaghel and T. Davis, Representations of Coulomb Friction for Dynamic Analysis, *Earthq. Eng. Struct. Dynam.*, 1997, **26**(5), p 541–548

27. M. Assidi, L. Fourment, S. Guerdoux, and T. Nelson, Friction Model for Friction Stir Welding Process Simulation: Calibrations from Welding Experiments, *Int. J. Mach. Tools Manuf*, 2010, **50**(2), p 143–155

28. ANSYS, I., *ANSYS® Fluent*,

29. M. Yu, W. Li, J. Li, and Y. Chao, Modelling of entire Friction Stir Welding Process by Explicit Finite Element Method, *Mater. Sci. Technol.*, 2012, **28**(7), p 812–817

30. H. Palaniswamy, G. Ngaile, and T. Altan, Finite Element Simulation of Magnesium Alloy Sheet Forming at Elevated Temperatures, *J. Mater. Process. Technol.*, 2004, **146**(1), p 52–60

31. K.C. Mills, *Recommended Values of Thermophysical Properties for Selected Commercial Alloys*, Chennai, Woodhead, 2002

32. P.D. Harvey, *Engineering Properties of Steel*, American Society for Metals Metals Park, Ohio, 1982

33. D.M. Neto, M.C. Oliveira, J.L. Alves, and L.F. Menezes, Influence of the Plastic Anisotropy Modelling in the Reverse Deep Drawing Process Simulation, *Mater. Des.*, 2014, **60**, p 368–379

34. W. Woo, Z. Feng, X.L. Wang, K. An, B. Clausen, T.A. Sisneros, and J.S. Jeong, In Situ Neutron Diffraction Analysis of Grain Structure During Friction Stir Processing of an Aluminum Alloy, *Mater. Lett.*, 2012, **85**, p 29–32

35. J.G. Kaufman, *Properties of Aluminum Alloys: Tensile, Creep, and Fatigue Data at High and Low Temperatures*, ASM International, New York, 1999

36. A. Bastier, M.H. Maitournam, K.D. Van, and F. Roger, Steady State Thermomechanical Modelling of Friction Stir welDing, *Sci. Technol. Weld. Join.*, 2006, **11**(3), p 278–288

37. U. Donatus, G.E. Thompson, X. Zhou, J. Wang, and K. Beamish, Flow Patterns in Friction Stir Welds of AA5083 and AA6082 Alloys, *Mater. Des.*, 2015, **83**, p 203–213

38. Y. Morisada, T. Imaizumi, H. Fujii, M. Matsushita, and R. Ikeda, Three-Dimensional Visualization of Material Flow During Friction Stir Welding of Steel and Aluminum, *J. Mater. Eng. Perform.*, 2014, **23**(11), p 4143–4147